Engineering Fracture Mechanics 320 (2025) 111075

Contents lists available at ScienceDirect

Engineering Fracture Mechanics

journal homepage: www.elsevier.com/locate/engfracmech

# Investigation on dynamic anisotropy of bedded shale under SHPB impact compression

Xianhui Feng [a], Bin Gong [b,*], Xiaofeng Cheng [c], Xu Chen [d], Xun Xi [a], Kaikai Wang [e]

[a] School of Civil and Resources Engineering, University of Science and Technology Beijing, Beijing 100083, China
[b] College of Engineering, Design and Physical Sciences, Brunel University of London, London UB8 3PH, UK
[c] College of Water Resources and Architectural Engineering, Northwest A&F University, Yangling 712100, China
[d] State Key Laboratory of Geohazard Prevention and Geoenvironment Protection, Chengdu University of Technology, Chengdu 610059, China
[e] State Key Laboratory of Coastal and Offshore Engineering, Dalian University of Technology, Dalian 116024, China

ARTICLE INFO

*Keywords:*
Shale failure
Bedding inclination
SHPB
Dynamic anisotropy
Strain rate effect

ABSTRACT

Revealing the fracture characteristics of shales under impact is significant for the exploitation and utilization of geological energy. In this study, the progressive failure process of bedded shale was tested by the dynamic Split Hopkinson Pressure Bar system and measured by the high-speed camera. Furthermore, their dynamic mechanical properties and fracture features under impact compression were comprehensively investigated. The results show that according to the triggering mechanisms of micro-cracks and mechanical factors governing fracture morphology, the failure patterns of shales can be categorized into five types: splitting failure along bedding plane, slip failure along bedding plane, mixed shear cracks between layers, tensile-shear mixed cracks, and tensile crack along bedding plane. Meanwhile, when the bedding angle $\theta = 0^\circ$, the sample experiences splitting failure, with acoustic emissions concentrated predominantly at horizontal bedding planes. When $\theta = 30^\circ$ and $60^\circ$, the sample experiences shear failure characterized by shear cracks, mixed shear cracks and multiple composite tensile-shear cracks. When $\theta = 90^\circ$, the sample exhibits tensile and splitting cracks. With increasing strain rate, the fracture pattern of the $60^\circ$ sample becomes dominated by slip and tensile-shear mixed cracks. With increasing peak stress intensity, the fracture modes of the $30^\circ$ and $60^\circ$ samples gradually transition from center-oriented failure towards shear failure along bedding planes. Additionally, for the $90^\circ$ specimen, as the shock wave intensifies, secondary splitting cracks emerge in matrix, indicative of a fracture pattern across bedding planes.

## 1. Introduction

Numerous geotechnical engineering endeavors, including engineering blasting, protective engineering, and seismic exploration, necessitate an intricate understanding of stress wave propagation and attenuation within layered rock masses, alongside the consequential deformation and failure dynamics under dynamic loads [1–3]. Shale behaves as a brittle material and exhibits brittle and semi-brittle response to peak strength load at different bedding inclinations [4–6]. The structural anisotropy of these formations not only dictates their dynamic mechanical characteristics but also engenders unique features in stress wave propagation and attenuation, diverging significantly from those observed in homogeneous rock masses, thereby adding layers of complexity and intricacy [7–10].

* Corresponding author.
*E-mail address:* bin.gong@brunel.ac.uk (B. Gong).

https://doi.org/10.1016/j.engfracmech.2025.111075
Received 31 July 2024; Received in revised form 14 February 2025; Accepted 23 March 2025
Available online 24 March 2025

**List of symbols**

| | |
|---|---|
| $\Theta$ | Bedding dip angle |
| $\varepsilon_r(t)$ | Reflected stress wave |
| $\sigma(t)$ | Stress |
| $\dot{\varepsilon}(t)$ | Strain rate |
| $E$ | Elastic modulus |
| $A$ | Cross-sectional area |
| $(x, y)$ | Coordinate of a pixel in the $xy$ plane |
| $f(x, y)$ | The initial grayscale value of the pixel $(x, y)$ |
| $f'(x, y)$ | The standardized grayscale value of the pixel $(x, y)$ |
| $\varepsilon_i(t)$ | Incident stress wave |
| $\varepsilon_t(t)$ | Transmitted stress wave |
| $\varepsilon(t)$ | Strain |
| $\nu(t)$ | Particle velocity |
| $C_0$ | Stress wave velocity |
| $L_s$ | Length of the specimen |

Shale anisotropy, stemming from variations in structural features, significantly influences failure mechanisms. It dictates the directionality and strength of rock properties, affecting fracture propagation, deformation behavior, and overall stability [11–13]. Anisotropic rocks exhibit different mechanical responses along various axes, leading to diverse failure patterns under stress conditions. These variations impact engineering projects, such as tunneling, mining, and slope stability assessments, requiring tailored approaches to mitigate risks associated with anisotropic rocks [14–16].

In recent years, there has been a surge in both experimental and theoretical investigations into the anisotropic mechanical characteristics of layered shales. Luo et al. [17] adapted a constitutive model to better anticipate shale strength under varying confining pressures. Expanding on this, Luo et al. [18] and Chao et al. [19] employed soft and hard laminated rock-like specimens to identify areas of crack initiation, particularly notable through Brazilian splitting tests. Furthermore, Zhang et al. [20] categorized the failure modes of Brazilian shale discs into three distinct types, highlighting a propensity for tensile failure along the bedding plane. Meanwhile, Kolawole and Oppong [21] devised effective micromechanical measures, shedding light on both micro- and macro-mechanical properties of shales. Zhang et al. [22] delved into the significance of shale heterogeneity, pinpointing it as a primary factor influencing the magnitude of critical pressures, as evidenced by extensive hydraulic fracturing tests on shales with differing bedding inclinations. In a related vein, Zhao et al. [23] unearthed distinct micromechanisms governing shale ductility under varying conditions of high confining pressure and temperature, elucidated through meticulous triaxial compression experiments on bedding shale specimens. However, the dynamic fracturing process involving crack creation and development is still challenging to be fully understood, and the caused influence on impact resistance of layered shales remains unclear.

As a complement to laboratory experiments, numerical simulation has emerged as a formidable tool for gaining a profound insight into the intricate mechanisms governing the failure of anisotropic and heterogeneous materials within layered rock formations. Zhou et al. [24] devised a numerical three-dimensional Split Hopkinson Pressure Bar (SHPB) test, employing a synergistic coupling of the particle flow code and fast Lagrangian analysis of continuum methods to faithfully replicate the laboratory behavior of shale specimens. Wu et al. [25] uncovered a nuanced crack evolution pattern which is characterized by a concave tendency, leading to a shift in failure mode from matrix-dominated to bedding-dominated. This pattern can be observed in bedding sandstone models housing two pre-existing flaws. Meanwhile, Zhai et al. [26] delved into the progressive failure dynamics and acoustic emission signatures of shales by employing the bonded-particle model integrated with the moment tensor algorithm. Notably, Wang et al. [27,28] introduced an innovative three-dimensional rough discrete fracture network (RDFN3D) model, offering a comprehensive framework to consolidate modeling approaches for complex structural planes, thereby enhancing the fidelity of numerical simulations in capturing real-world behaviors. However, the traditional numerical technologies show limitations in characterizing the continuous initiation, propagation and coalescence of cracks induced by the progressive stress process involving stress buildup, stress release and stress redistribution.

Given the intricate mechanical dynamics inherent in layered rock masses and the notable advantages offered by numerical simulation techniques, this study employs the SHPB system test to delve into the influence of bedding inclinations and shock waves on the initiation and propagation of cracks within shales. Furthermore, it endeavors to elucidate the failure process and underlying mechanisms of bedded shales when subjected to dynamic impacts. To unveil the nuanced mechanical intricacies governing shale failure characteristics, the study employs the rock failure process analysis (RFPA) method alongside the digital image processing techniques. This integrated approach facilitates a meticulous recreation of the entire lifecycle of crack initiation, propagation, and penetration within the underlying rock mass model under dynamic impact loads. Through systematic analysis, the study aims to unearth fundamental principles and laws governing these processes, thereby furnishing essential data and a robust theoretical framework for comprehending the large-scale engineering stability of layered rock masses.

## 2. Experimental setup and process

### 2.1. Sample preparation

The specimens utilized in this study were sourced from the Lu Mountain Mine located in Jiujiang City in Jiangxi Province, China. The stratified rock reservoir within this region showcases well-defined layering and prominent structural stratifications. Through the sufficient technical demonstrations, it has been ensured that the sampling point selected for the physical test exhibits good representativeness, and the integrity of the extracted shale can be guaranteed. In Fig. 1(a), a close-up view of clay minerals reveals discernible primary defects, notably microcracks, indicative of the inherent heterogeneity of the rock. Fig. 1(b) illustrates the formation of weak planes resulting from the parallel proliferation of microcracks amidst plate-like minerals, which form the vulnerable surfaces of the specimens. Meanwhile, Fig. 1(c) depicts clastic minerals filling the interstices between clay minerals, aligning themselves parallel to the bedding planes. In essence, the shale specimens chosen for this study exhibit a fissile structure at the microscopic scale and a clearly defined layering structure at the macroscopic level, characteristic of layered rock formations.

To procure specimens with varied bedding dip angles, we firstly defined the bedding dip angle $\theta$ as the angle between the bedding plane direction and the horizontal baseline. Then, by utilizing the drill bit with the diameter of 50 mm, the samples were cored in the directions spanning 0°, 30°, 60°, and 90°, as shown in Fig. 2. Adhering to the standards set forth by the International Society for Rock Mechanics and Rock Engineering [29], the samples underwent processing into cylindrical forms, with a diameter of 48 mm and a height of 50 mm, as illustrated in Fig. 3.

### 2.2. Testing apparatus and methodology

The SHPB test system [30–32] utilized in this study comprises three key components, *i.e.*, the dynamic impact system, the stress propagation system, and the signal and data processing system, as depicted in Fig. 4. In the experimental setup, the incident bar, transmission bar, absorption bar, and striker were all constructed from silicon-manganese steel, boasting a diameter of 50 mm, a density of 7,850 kg/m$^3$, and a longitudinal wave speed of 5,201 m/s. The incident bar spans a length of 3.0 m, while the absorption bar and transmission bar measure 1.8 m and 0.5 m in length, respectively.

The dynamic test system incorporates cutting-edge instrumentation, including a super-dynamic strain gauge (CS-ID), an oscilloscope (DL-750), and a strain gauge model (BX120-2AA), facilitating precise measurement and analysis of stress and strain during the impact process. To visually capture the dynamic failure process of a specimen, the digital image real-time monitoring system is employed, comprising a high-speed camera and a high-intensity light source. This system can capture images at intervals of 10 μs, offering invaluable insights into the evolution of cracks and deformation patterns during the experiment.

Due to the difference in wave impedance between the pressure rod and the tested specimen, the incident stress wave undergoes reflection and transmission at the interface between them. Upon impact, a portion of the stress wave reflects into the incident rod, while the remaining energy propagates through the specimen to the transmission rod, thereby completing the loading sequence, as illustrated in Fig. 5. The strain gauges affixed to the midpoints of both the incident and transmission rods facilitate the measurement of stress wave propagation components. Specifically, the strain gauge attached to the incident rod captures the incident stress wave signal, denoted as $\varepsilon_i(t)$, along with the reflected stress wave signal $\varepsilon_r(t)$, while the strain gauge on the transmission rod records the transmitted stress wave signal $\varepsilon_t(t)$.

Designating the contact point between the incident rod and the specimen as $X_1$, and the corresponding contact point between the transmission rod and the specimen as $X_2$, we can examine the propagation of stress waves in the pressure rod. Throughout the experiment, stress waves within the pressure rod consistently exhibit elastic behavior. At the critical points $X_1$ and $X_2$, both stress and particle velocity are measured to elucidate the dynamic response of the system as follows:

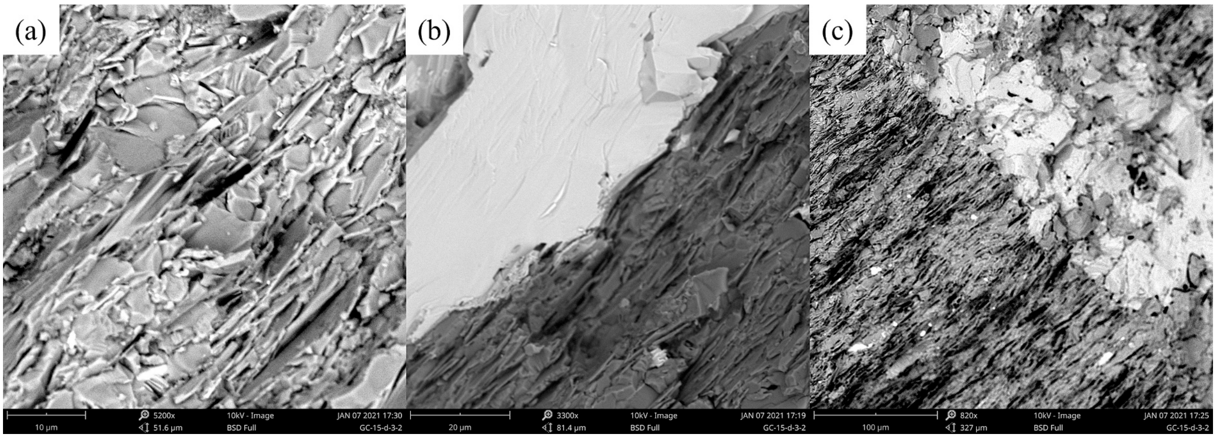


**Fig. 1.** Shale micrograph obtained by the scanning electron microscope (QUANTA450).

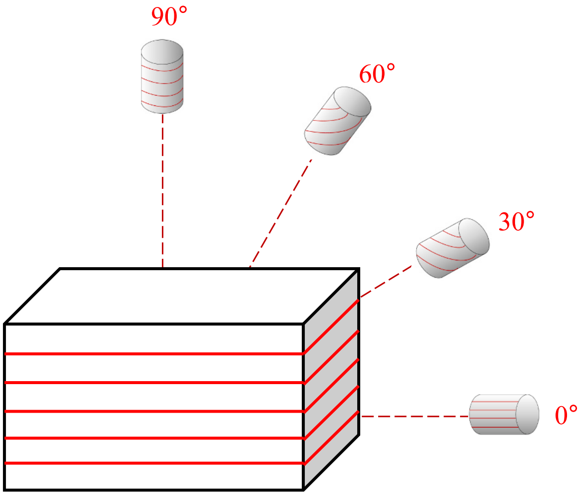


**Fig. 2.** Shale coring schematic.

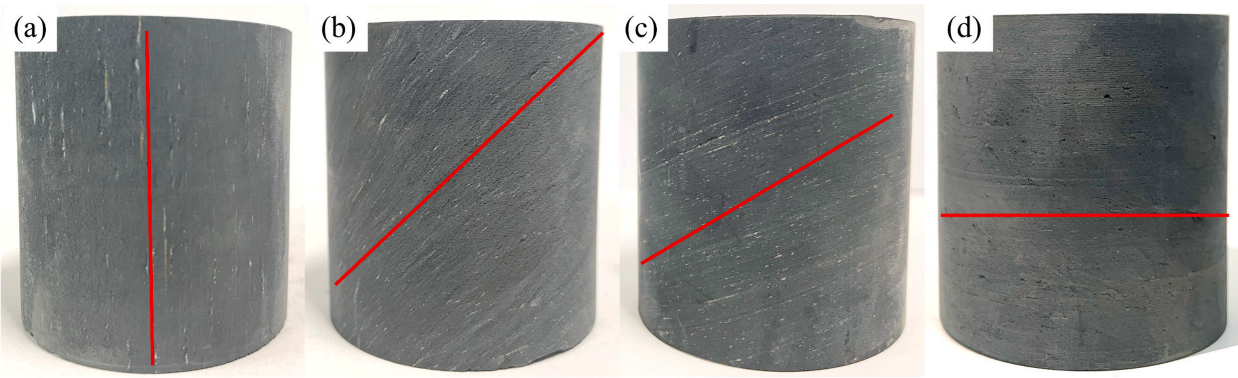


**Fig. 3.** Representative shale specimens with (a) $\theta = 0^\circ$, (b) $\theta = 30^\circ$, (c) $\theta = 60^\circ$ and (d) $\theta = 90^\circ$.

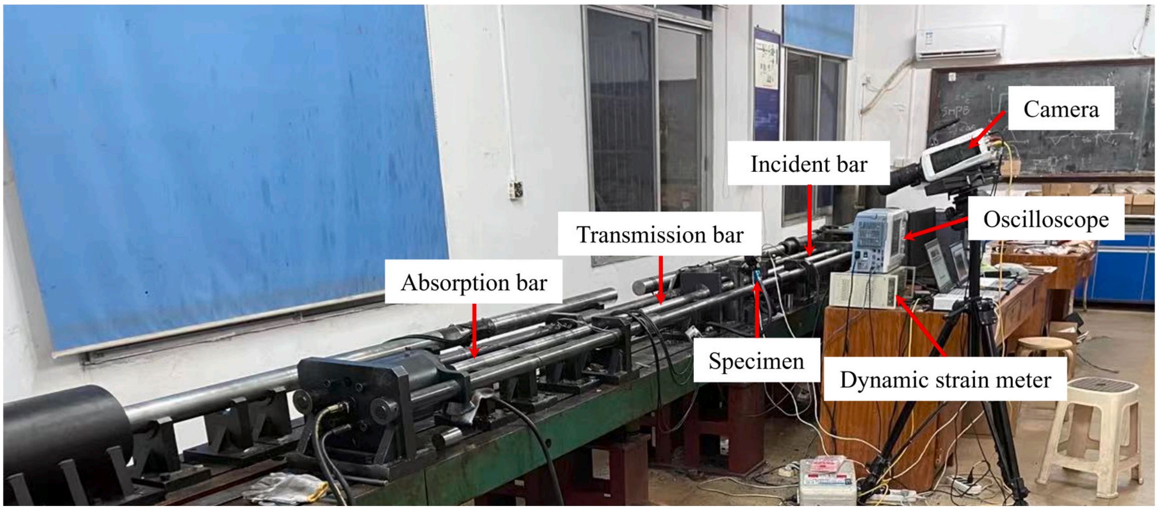


**Fig. 4.** The SHPB system device schematic.

$$\sigma_1(t) = \sigma_1(t) + \sigma_R(t) = E(\varepsilon_1(t) + \varepsilon_R(t)) \tag{1}$$

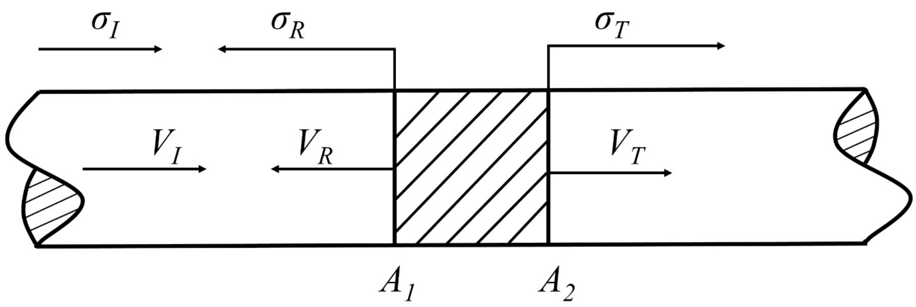


**Fig. 5.** Effect of stress wave on the interface between bar and specimen.

$$v_1(t) = v_1(t) + v_R(t) = C_0(\varepsilon_1(t) - \varepsilon_R(t)) \tag{2}$$

$$\sigma_2(t) = \sigma_T(t) = E\varepsilon_T(t) \tag{3}$$

$$v_2(t) = v_T(t) = C_0\varepsilon_T(t) \tag{4}$$

where $\sigma_1(t)$ and $\nu_1(t)$ represent the stress and particle velocity at Point $X_1$, respectively, and $\sigma_2(t)$ and $\nu_2(t)$ represent the stress and particle velocity at Point $X_2$, respectively. $E$ and $C_0$ are the elastic modulus and stress wave velocity of the pressure rod, respectively.

Referring to the equation provided, the average stress $\sigma(t)$, strain rate $\dot{\varepsilon}(t)$, and strain $\varepsilon(t)$ of the specimen can be derived throughout the loading process as follows:

$$\sigma(t) = \frac{EA_0}{2A_s}(\varepsilon_I(t) + \varepsilon_R(t) + \varepsilon_T(t)) = \frac{EA_0}{A_s}\varepsilon_T(t) \tag{5}$$

$$\dot{\varepsilon}(t) = \frac{C_0}{L_s}\varepsilon_I(t) - \varepsilon_R(t) - \varepsilon_T(t) = -\frac{2C_0}{L_s}\varepsilon_R(t) \tag{6}$$

$$\varepsilon(t) = \int_0^t \dot{\varepsilon}(t)dt = \frac{2C_0}{L_s}\int_0^t \varepsilon_R(t)dt \tag{7}$$

where the variables $A_0$ and $A_s$ represent the cross-sectional areas of the loading rod and the sample, respectively, while $L_s$ represents the length of the specimen. The variables $\sigma_I(t)$, $\sigma_R(t)$, and $\sigma_T(t)$ denote the incident stress, reflected stress, and transmitted stress at time $t$, respectively.

## 3. Experimental results

### 3.1. Stress equilibrium analysis

Fig. 6 illustrates the dynamic stresses applied to a representative specimen. Throughout the dynamic testing phase, the summation

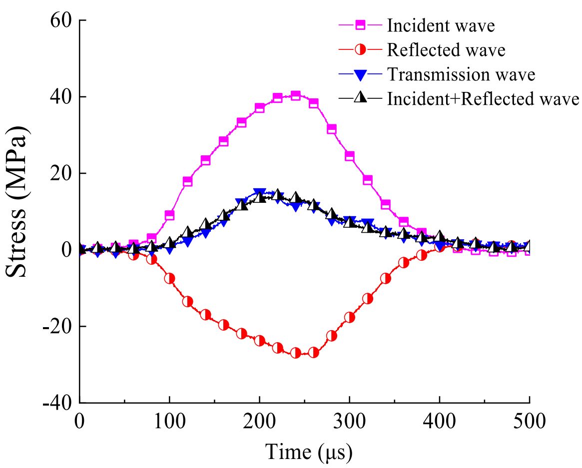


**Fig. 6.** The dynamic equilibrium state reached in test.

of the incident stress wave and the reflected stress wave closely approximated the transmitted stress wave. This observation suggests a near-perfect attainment of stress equilibrium, thereby ensuring the efficacy and reliability of the dynamic testing procedure.

In Fig. 7, the stress–strain curves of the shale specimens subjected to dynamic compression loads are depicted, and each corresponds to one bedding angle. Clearly, the dynamic stress–strain curves of shale can be basically divided into four stages: compaction, elasticity, yielding and failure. In the elastic stage, the stress–strain curve increases nearly linearly, and the stress is proportional to the strain. In the yielding stage, the dynamic curve becomes flat, and the internal cracks of the specimen gradually propagate. After the specimen reaches the peak strength, the internal cracks penetrate to form the macroscopic failure. Simultaneously, the disparities in peak stress level can be observed. The different curve characteristics for each bedding angle indicate the significant anisotropy of bedded shale.

### 3.2. Failure characteristics

During the dynamic impact compression testing, the high-speed camera was employed to meticulously capture the fracture process unfolding within the specimens. Upon the impact of the stress wave, an instantaneous release of energy reverberates through the stratified rock, often accompanied by a distinctive loud noise. This pivotal moment heralds the rapid formation of macroscopic cracks within the rock, swiftly propagating through the specimen. As these cracks proliferate, the load-bearing capacity of the specimen diminishes precipitously, culminating in the formation of a fracture surface.

Fig. 8 shows the dynamic crack propagation processes of the shale specimens with distinct bedding angles. These images vividly portray the morphological variances in failure modes, underscoring the pronounced anisotropy inherent in shale materials. For the 0° specimen, we can see that an initial horizontal crack emerges along the bedding plane, extending parallel to the axial loading direction. By 140 μs, this crack evolves into a macroscopic fissure spanning the specimen's length, indicative of a typical cleavage failure process. In contrast, the 30° specimen manifests initial shear cracks along the bedding plane upon the initial impact load, with these cracks extending towards both ends of the specimen. This results in a predominately shear-dominated tensile-shear mixed failure characteristic. At 90 μs after impact, the 60° specimen displays an initial shear crack along the bedding plane, further propagating into a macroscopic fissure along the same plane, exhibiting a characteristic shear failure along the bedding plane. Lastly, the 90° bedded specimen exhibits an initial crack along the bedding plane. As the shock wave intensifies, secondary splitting cracks emerge in the matrix, indicative of a fracture pattern across the bedding planes.

### 3.3. Failure pattern and strain rate effect

Throughout the experiment, the high-speed photography served to chronicle the dynamic failure modes exhibited by the bedded shale specimens. Through the meticulous analysis of the spatial correlation between the macroscopic fracture cracks and bedding planes, the failure patterns observed in the shale specimens under impact compression can be mainly categorized into five distinct types as illustrated Fig. 9, *i.e.*, (a) splitting failure along the bedding plane (Type I); (b) slip failure along the bedding plane (Type II); (c) mixed shear cracks between layers (Type III); (d) tensile-shear mixed cracks (Type IV); (e) tensile crack along the bedding plane (Type V).

Fig. 10 illustrates the impact fracture features of shale specimens with different bedding angles under various strain rates, in which Series (a), (b), (c) and (d) are for the specimens with $\theta = 0°$, 30°, 60° and 90°, respectively. Meanwhile, Series (1), (2), (3) and (4) correspond to the strain rate = 20 $s^{-1}$, 50 $s^{-1}$, 80 $s^{-1}$, and 100 $s^{-1}$, respectively. From Fig. 10, it is clear that the fracture behaviors of the shale specimens vary significantly depending on their bedding angles. The 0° specimens consistently present a relatively uniform

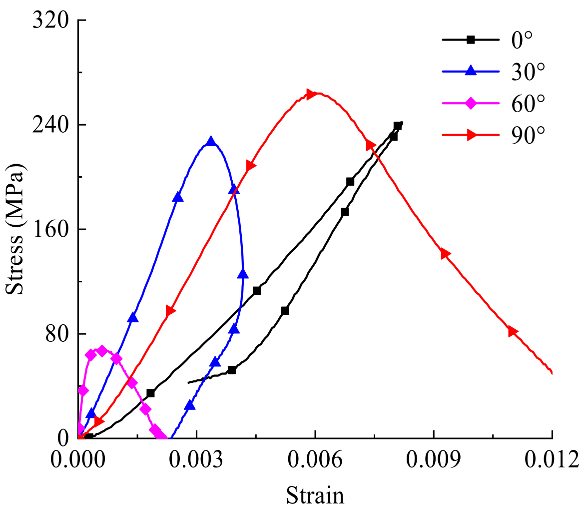


**Fig. 7.** Dynamic stress–strain curves of the shale specimens with different bedding angles.

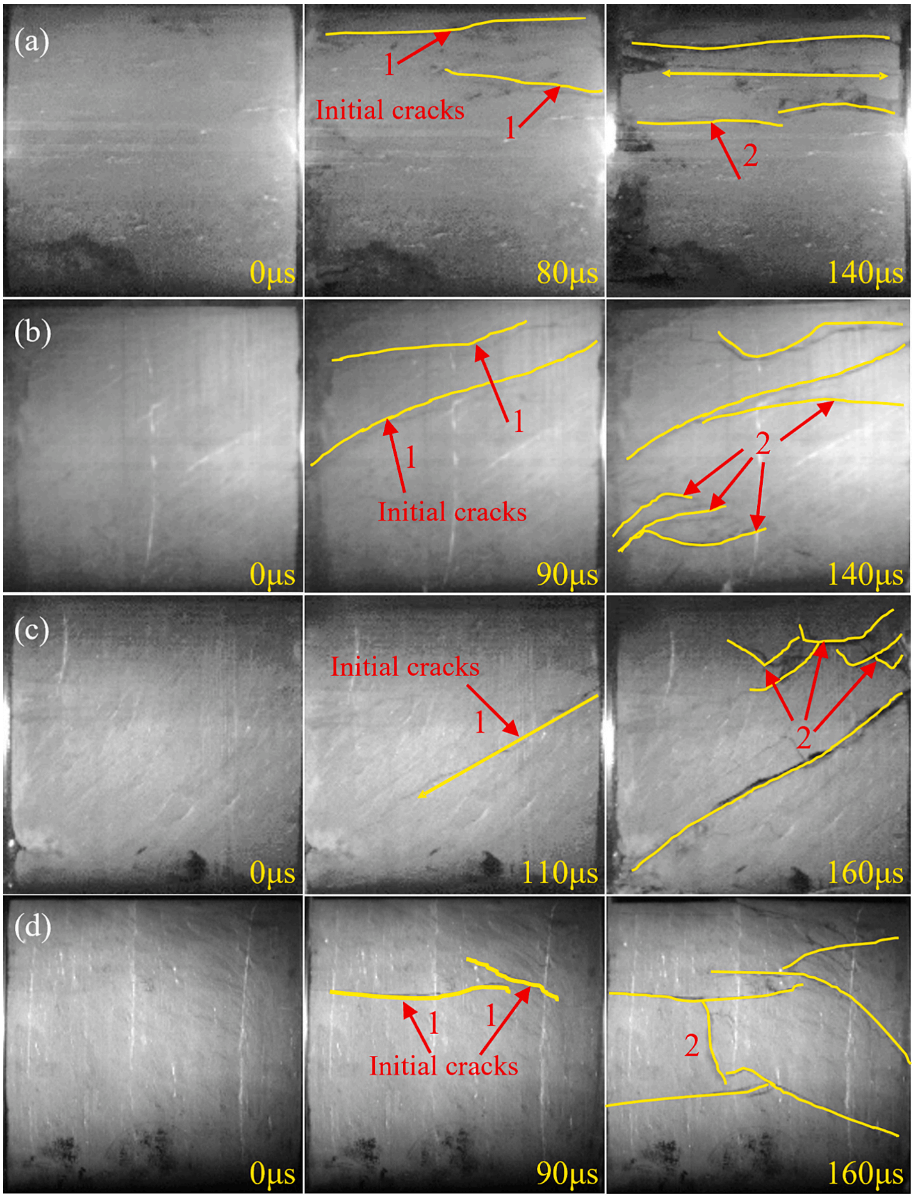


**Fig. 8.** Impact compression testing processes of the specimens with various bedding angles: (a) $\theta = 0^{\circ}$, (b) $\theta = 30^{\circ}$, (c) $\theta = 60^{\circ}$ and (d) $\theta = 90^{\circ}$.

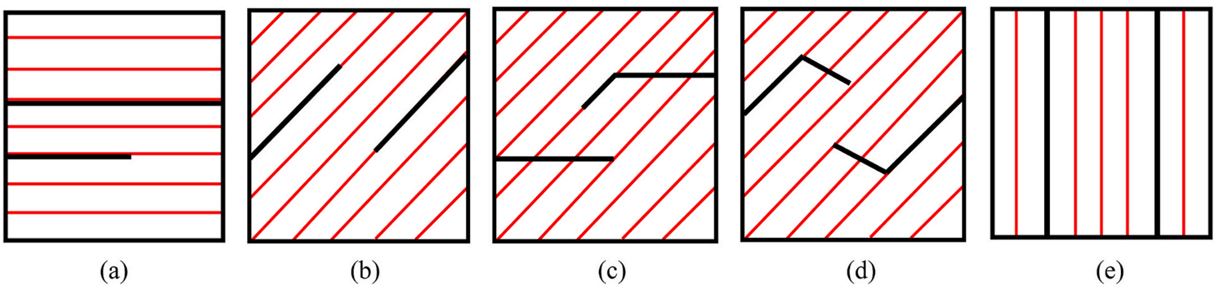


**Fig. 9.** Classification of failure patterns of shales under impact compression: (a) splitting failure along the bedding plane, (b) slip failure along the bedding plane, (c) mixed shear cracks between layers, (d) tensile-shear mixed cracks and (e) tensile crack along the bedding plane.

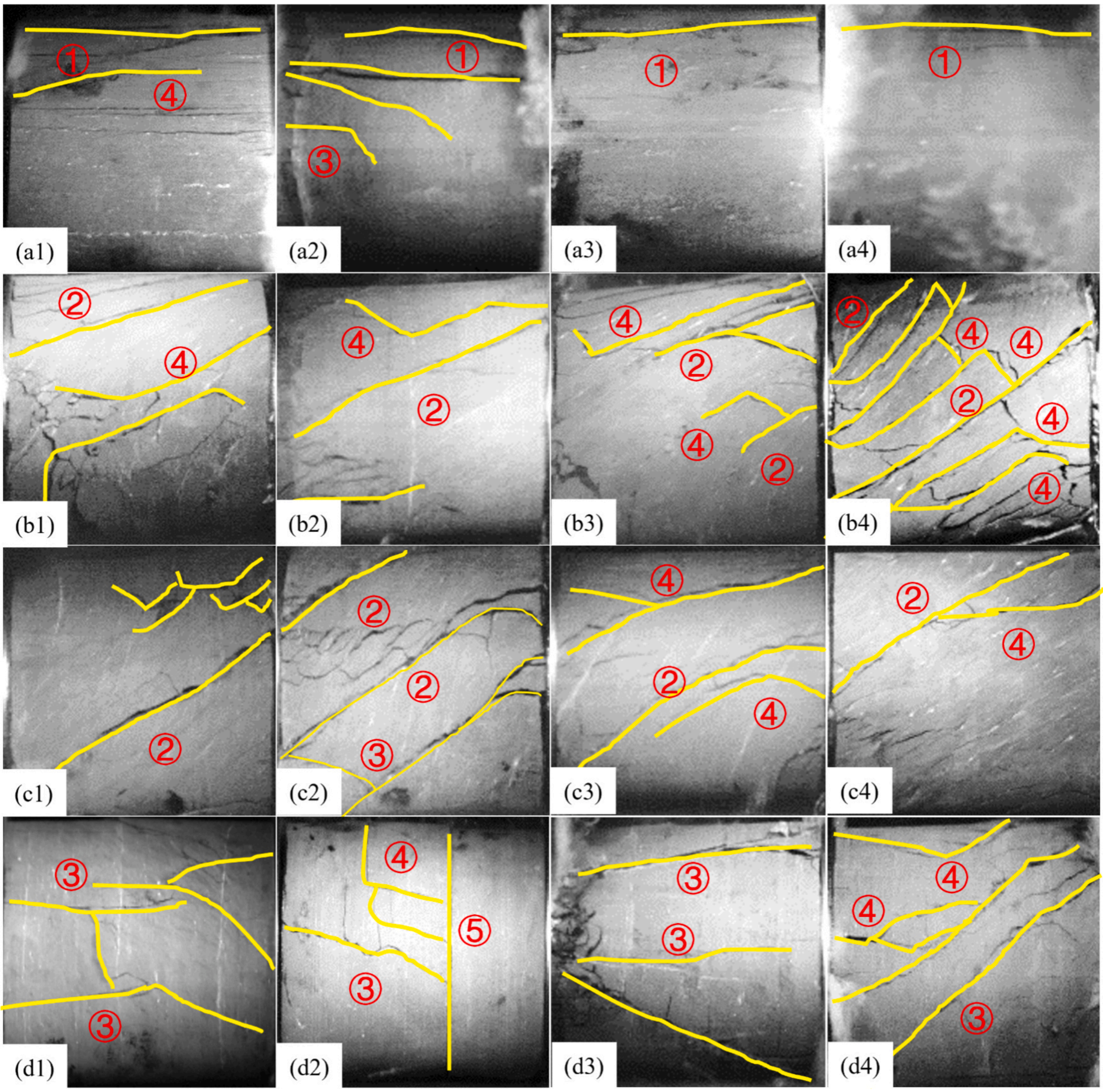


**Fig. 10.** Impact compression failure features of shales: Series (a), (b), (c) and (d) are for the specimens with $\theta = 0^{\circ}$, 30°, 60° and 90°, respectively; Series (1), (2), (3) and (4) correspond to the strain rate = 20 $s^{-1}$, 50 $s^{-1}$, 80 $s^{-1}$, and 100 $s^{-1}$, respectively.

fracture mode, predominantly showcasing a splitting pattern along the horizontal bedding plane, with the fracture surfaces extending along the axial direction. This fracture type is characterized by the penetration of the matrix along the weak bedding plane (Type I). Conversely, the 30° specimens exhibit shear cracks along the bedding planes at both ends (Type II), with the fracture surfaces penetrating the entire shale samples. Fig. 10(b4) shows that when the strain rate = 100 $s^{-1}$, the shale specimen displays a primary crack along the bedding plane and multiple composite tensile-shear cracks (Type IV), penetrating both the bedding planes and the matrix. Notably, the 30° specimen demonstrates coexisting splitting tensile and shear cracks under the four strain rate conditions. In contrast, the fracture patterns of the 60° specimens lack consistency. Specifically, when the specimen is subject to the strain rate of 20 $s^{-1}$, the fracture surface primarily extends along the bedding plane with shear cracks (Type II). However, when the strain rate increases to 50 $s^{-1}$, shear cracking prevails, accompanied by tensile cracks during the testing process (Type II and Type III). With the strain rate continuously increasing, the fracture pattern becomes dominated by a combination of Type II and Type IV cracks. Moreover, all the Type II and Type IV cracks coexist across the four strain rates. Besides, when the shale specimen with a 90° bedding angle is subject to a strain rate of 20 $s^{-1}$, two Type III tensile cracks penetrate the entire specimen. When the strain rate increases to 50 $s^{-1}$, the Type I tensile cracks are produced along the 90° bedding planes at the transmission end and one Type V tensile crack can also be observed. With the continuous growth of loaded strain rate, the shale exhibits splitting tensile fracture penetrating the matrix and the bedding plane along the loading direction. Finally, when the strain rate equals 100 $s^{-1}$, the large-angle tensile-shear fractures can be measured, penetrating both the matrix and the bedding plane at the loading ends. Simultaneously, the fracture surfaces evolve through multiple bedding planes towards the center of the specimen.

## 4. Numerical modeling

To further elucidate the mechanical mechanisms underlying the fracture features of shale, the RFPA method was integrated with the digital image processing techniques to characterize stress/strain variations and accurately simulate the progressive failure process of shale samples. Given that shales, as heterogeneous materials, contain a variety of granular media, pores, micro-cracks, and other inherent defects, their mechanical behaviors are intricately linked to their internal *meso*-structure. This includes factors such as stress distribution, crack propagation, damage evolution, and failure modes, all of which play a critical role in determining the overall mechanical response of the material.

### 4.1. Determination of material segmentation threshold

In this study, the image threshold segmentation technique was used to identify the shapes and positions of beddings and rock matrix and to divide the finite element mesh [33,34]. The geometric models for the image segmentation and parameter selection were constructed according to the features of actual rocks [35,36]. Gray-scale images generally adopt gray-scale histogram to determine the segmentation thresholds. The gray level histogram is a function related to gray level, which depicts the quantity of pixels possessing the specific gray level in the image. Here, the horizontal coordinate represents the gray level, while the vertical coordinate indicates the frequency of the gray level. In rock images, the gray values of adjacent pixels within the same mesoscale medium are relatively similar. However, the gray values of pixels in different mesoscale media show significant differences. This is reflected in the histogram, where distinct targets or backgrounds correspond to separate peaks. The selected segmentation thresholds are positioned in the valley between two adjacent peaks of the histogram to effectively separate the peaks.

The diverse microstructures can be effectively identified by applying varying grey thresholds, *i.e.*, different material types can be determined. The theoretical principles of the threshold calculation are represented by Eq. (8).

$$f^{'}(x,y)=\begin{cases}1/(\mathrm{n}+1) & f(x,y)\leqslant T_1\\ 2/(\mathrm{n}+1) & T_1<f(x,y)\leqslant T_2\\ \vdots & \cdots\\ \mathrm{n}/(\mathrm{n}+1) & T_{n-1}<f(x,y)\leqslant T_n\\ (\mathrm{n}+1)/(\mathrm{n}+1) & f(x,y)>T_n\end{cases}\tag{8}$$

Meanwhile, when the grayscale value of a pixel is less than or equal to the threshold $T_1$, it will be set to $1/(\mathrm{n}+1)$; if the grayscale value of pixel is greater than the threshold $T_n$, its grayscale function will be set to 1. Moreover, $f(x, y)$ represents the initial grayscale value of the pixel $(x, y)$, and $f'(x, y)$ represents the standardized grayscale value of the pixel $(x, y)$. The grayscale grid at the specific region of the shale model and the grayscale values along the line AA′ are shown in Fig. 11.

### 4.2. Elastic damage model for mesoscopic elements

The progressive failure process of a rock model under loading can be effectively described using damage mechanics. The elastic modulus of a damaged material is defined as:

$$E=(1-\omega)E_0\tag{9}$$

where $\boldsymbol{\omega}$ denotes the damage variable. $\boldsymbol{E}$ and $\boldsymbol{E}_0$ represent the elastic moduli of the damaged and undamaged materials, respectively. The constitutive relationships of the elements under uniaxial compression and tension are characterized by an elastic-brittle-plastic response [37]. Specifically, the constitutive relationship of a mesoscopic element under uniaxial tension can be expressed as:

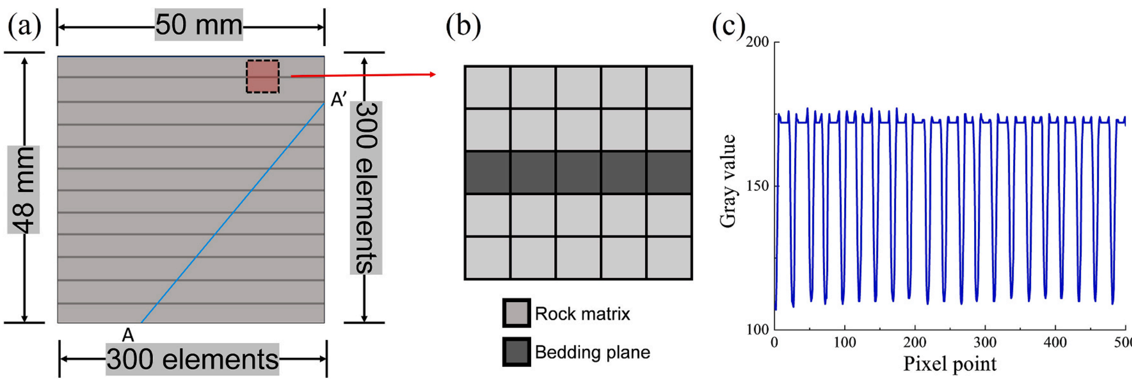


**Fig. 11.** The digital image processing: (a) the captured image, (b) the generated grayscale grid and (c) the grayscale values along the line AA′.

$$\omega = \begin{cases} 0 & \varepsilon > \varepsilon_{t0} \\ 1 - \dfrac{\lambda \varepsilon_{t0}}{\varepsilon} & \varepsilon_{tu} < \varepsilon \leq \varepsilon_{t0} \\ 1 & \varepsilon \leq \varepsilon_{tu} \end{cases} \tag{10}$$

where $\lambda$ is defined as the ratio between the residual tensile strength $f_{tr}$ and the initial tensile strength $f_{t0}$ and termed the residual strength coefficient. $\varepsilon_{t0}$ and $\varepsilon_{tu}$ represent the strain at the elastic tensile limit and the ultimate tensile strain, respectively. There is a correlation between them, *i.e.*, $\varepsilon_{tu} = \eta\, \varepsilon_{t0}$, where $\eta$ is the ultimate strain coefficient.

To investigate the damage of elements under a compression-shear stress state, the Mohr-Coulomb criterion is employed to determine the compression-shear failure point. This criterion is expressed as:

$$F = \sigma_1 - \frac{1 + sin\varphi}{1 - sin\varphi}\sigma_3 \geq f_{c0} \tag{11}$$

where $\sigma_1$ and $\sigma_3$ represent the major and minor principal stresses, respectively. $f_{c0}$ and $\varphi$ are the uniaxial compressive strength and the internal friction angle, respectively. When the element is under uniaxial compression and damaged according to the Mohr-Coulomb criterion, the damage variable $\omega$ can be similarly described as:

$$\omega = \begin{cases} 0 & \varepsilon > \varepsilon_{c0} \\ 1 - \dfrac{\lambda \varepsilon_{c0}}{\varepsilon} & \varepsilon \geq \varepsilon_{c0} \end{cases} \tag{12}$$

where $\lambda$ is the residual strength coefficient.

### 4.3. Model configuration

Based on the statistical damage mechanics, the RFPA method is able to characterize the progressive cracking behaviors of rock mass [38–40]. RFPA has been validated by researchers in modelling rock fracture [37,41,42] and was used for simulation in this study. In the impact load test, a conical bullet head was employed, generating a waveform akin to a sine wave. Among various waveforms, the triangle wave closely resembles the actual wave utilized in the experiment. Hence, a triangle wave was adopted for numerical simulation. In this section, the model dimensions were set at 50 mm × 48 mm and was divided into 300 × 300 elements, employing a two-dimensional plane strain constrains for computation as shown in Fig. 12. A triangle wave was utilized to impact the loading plate over the loading duration of 100 μs. Considering that there were many microjoints and microcracks inside the rock mass, which belong to non-uniform materials, the material non-uniformity was characterized by the Weibull distribution [43,44]. The related physical and mechanical parameters are detailed in Table 1. To ensure computational accuracy, a step-in-step analysis procedure was employed with the specific parameter configurations outlined in the table, meaning that the fine cracking process within one-time step can be captures in several sub-time steps. To comprehensively investigate the impact fracture morphology characteristics of shales, four distinct bedding angles were taken into account, *i.e.*, 0°, 30°, 60°, and 90°. In addition, the numerical simulations were conducted in alignment with the above physical experiments.

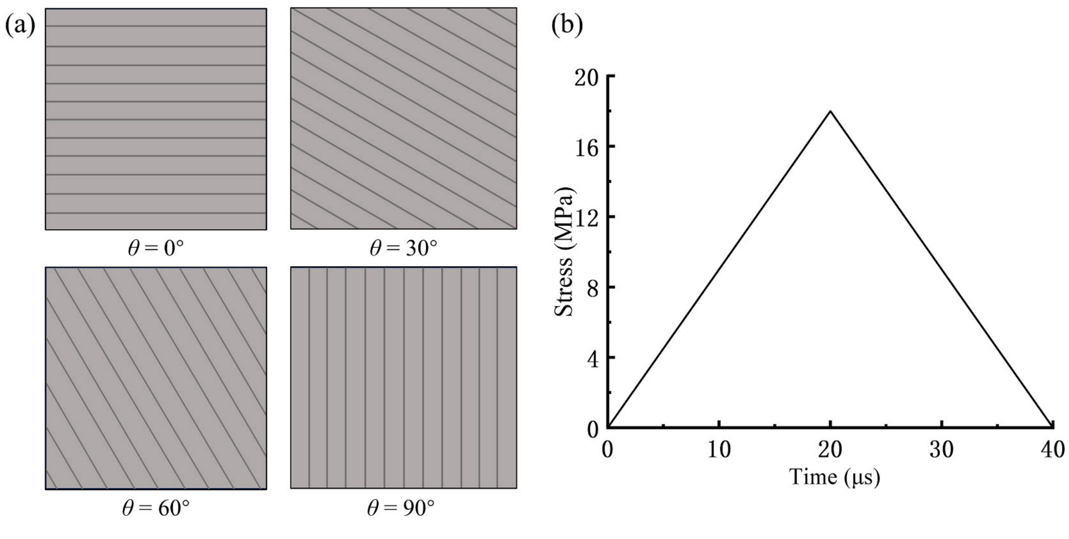


**Fig. 12.** Numerical modeling: (a) the models with various bedding angles and (b) the triangle wave for impact loading.

**Table 1**
physical and mechanical parameters for simulation.

| Parameter | Bedding plane | Matrix |
|---|---|---|
| Density (kg/m$^3$) | 2,500 | 2,500 |
| Young's modulus (GPa) | 5 | 50 |
| Poisson's ratio | 0.2 | 0.2 |
| Homogeneity index | 3 | 8 |
| Unixial compressive strength (MPa) | 50 | 100 |

## 5. Numerical results

### 5.1. Simulation of SHPB test

Fig. 13 indicates the failure processes of the models with varying bedding angles under dynamic impact compression, where the maximum shear stress contours and acoustic emission fields are presented. The results demonstrate that each AE event corresponds to the failure of an element within the shale model, with the number of AE events being directly proportional to the number of failed elements. In the figure, red circles represent AE events associated with tensile failure of elements, while white circles denote AE events resulting from compressive-shear failure. The radius of each circle is proportional to the energy released during the failure event [45,46]. Regions with denser clusters of circles indicate higher levels of element damage. Besides, the center and radius of the circles correspond to the spatial locations and energy magnitudes of the AE events within the acoustic emission fields. The labels M and A represent the contours of maximum shear stress and the acoustic emission fields, respectively, while the numbers 0, 30, 60, and 90 indicate bedding dip angles of 0°, 30°, 60°, and 90°, respectively. This visualization provides valuable insights into the spatial distribution and energy characteristics of damage during the shale failure process.

For the 0° bedded model, the initial appearance of damaged elements is observed at the incident. As the impact loading progresses, the shale specimen proceeds to develop a through crack along the bedding plane, extending further along the middle beddings from the initial crack. This numerical simulation outcome concurs with the dynamic impact failure mode exhibited by the related shale sample in Fig. 10, characterized by the Type I failure with the failure surface opening along the bedding plane. During the initial stage of impact loading for the 30° and 60° bedded specimens, the micro-cracks occur along the bedding planes near the incident end, concurrently with noticeable damage along the bedding planes. Subsequently, as the impact loading progresses, the models experience shear cracks (Type II) and multiple composite tensile-shear cracks (Type IV) along the bedding planes and across the matrix. This simulated result also aligns with the experimental findings of the corresponding shale sample, where damage across the inclined beddings was observed.

For the 60° model, the noticeable damage is evident at the edge of the incident end during the initial loading stage. Subsequently, in the later stages of loading, the macroscopic crack formation in the rock sample is primarily dominated by shear cracks, accompanied by tensile cracks. The failure mode can be characterized by Type II, Type III and Type IV cracks, with multiple composite compressive-shear and tensile-shear cracks emerging along the inclined beddings at the center. This outcome closely resembles the physical test data, where the central portion of the sample undergoes a mixed fracture mode crossing the bedding planes. When the bedding angle increases to 90°, tensile fractures happen along the vertical beddings at the middle and right side of the sample because of the tensile wave produced by the superposition of incident stress wave and reflected stress wave. This phenomenon can also be observed in Fig. 10 (d2).

### 5.2. Effect of stress wave on rock fracture

Both the physical experiment and numerical simulation tests have revealed the pronounced influence of bedding angle and peak strength on the failure characteristics of the samples. Consequently, this section further employs the simulation scenarios at $\theta = 0°$, 30°, 60°, and 90° to meticulously investigate the interplay between peak strength, bedding angle, and the resulting failure morphology of shale samples. Maintaining consistency, the model dimensions and mesh configurations align with those utilized above. The loading waveforms corresponding to these scenarios are illustrated in Fig. 14.

Fig. 15 depicts the fracture patterns observed in shale samples subjected to various bedding angles and impact waves. When the bedding angle is 0°, fractures primarily manifest as Type I cracks, closely resembling the experimental outcomes illustrated in Fig. 10. Meanwhile, when the bedding angle is equal to 30°, the numerical simulation result of Fig. 15(b3) mirrors the characteristics of impact test Fig. 10(b3), with slip cracks along the bedding plane and a prevalence of inter-layer mixed shear cracks shaping the macroscopic fissures. Similarly, the result Fig. 15(b4) aligns with impact test Fig. 10(b4), wherein Type II shear cracks emerge at the sample ends alongside multiple Type IV composite tensile-shear damage cracks traversing the bedding plane and penetrating the matrix. When the bedding angle rises up to 60°, the fracture modes captured in numerical simulations reflect the records of impact tests, emphasizing Type II shear cracks, Type III mixed shear cracks and Type IV tensile-shear mixed cracks as dominant features. They exhibit a distribution and composition akin to those observed in physical experiments. At a 90° bedding angle, all four numerical models yield analogous outcomes characterized by Type V tensile cracks. This simulation result bears resemblance to fracture outcome Fig. 10(d2) from impact testing.

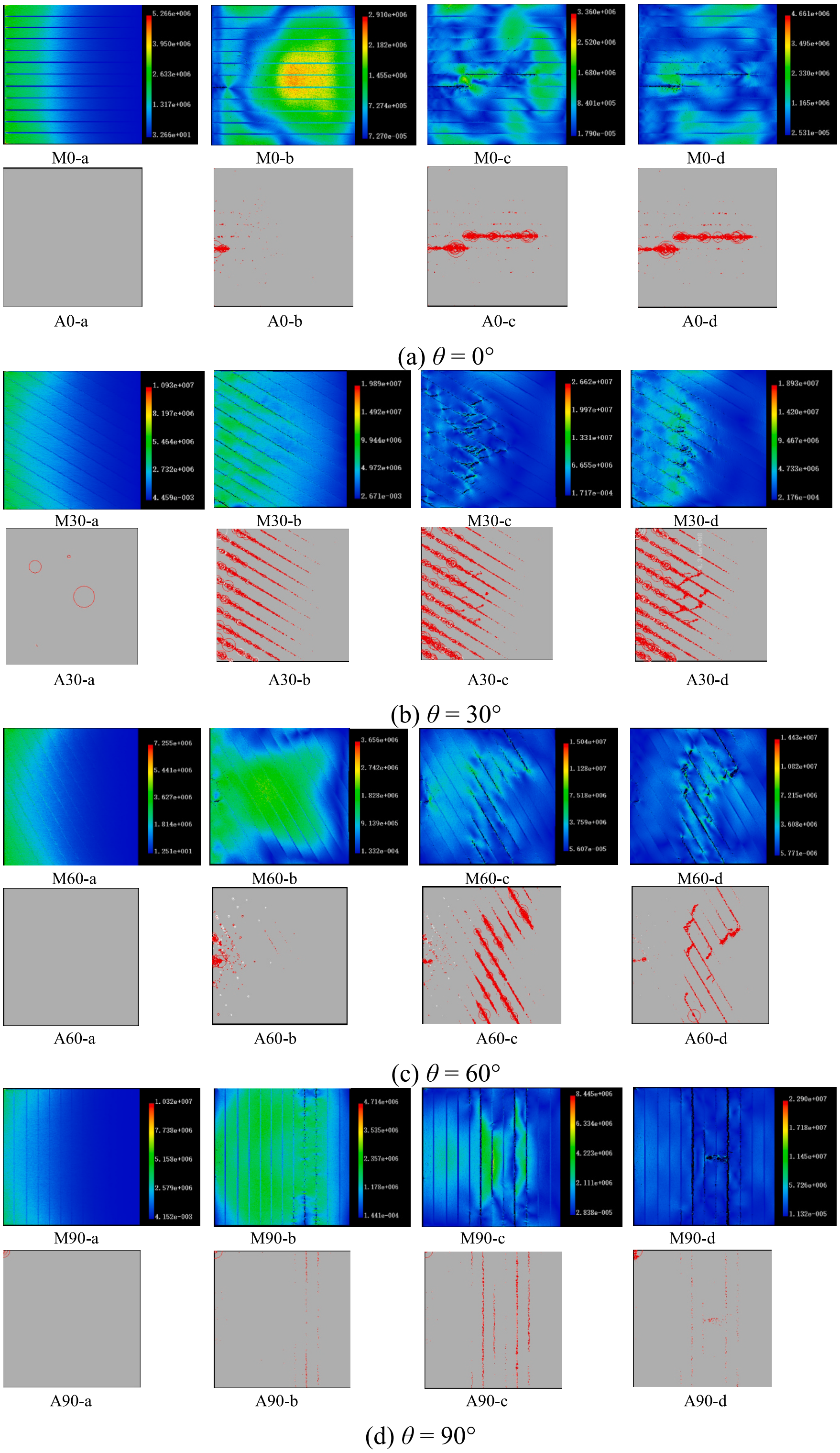


**Fig. 13.** Failure processes of the impact compression models when the bedding angle $\theta$ equals (a) 0°, (b) 30°, (c) 60° and (d) 90°.

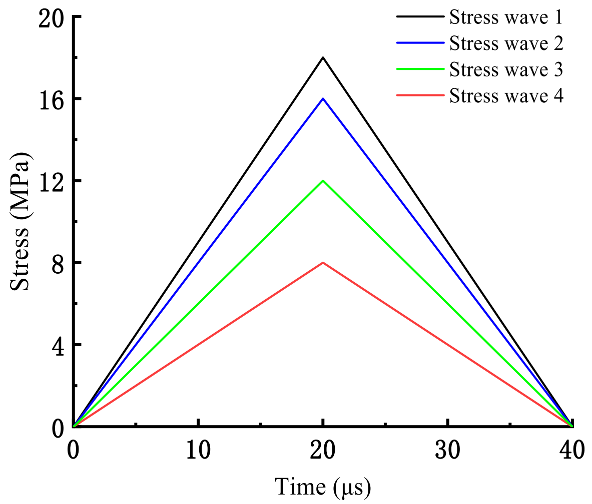


**Fig. 14.** Dynamic impact compressive stress waves.

### 5.3. Effect of bedding inclination on rock fracture

Many geotechnical engineering projects, including engineering blasting and protective projects, hinge on understanding the dynamics of stress wave propagation, superposition and attenuation within layered rock formations. As illustrated in Fig. 16, when the bedding angle $\theta = 0^\circ$, the model experiences a splitting failure that penetrates the bedding planes, with acoustic emissions concentrated predominantly at the horizontal bedding planes situated centrally within the sample. The distribution of macroscopic cracks appears relatively straightforward, predominantly showcasing Type I fissures elongating along the weakened bedding planes.

When the bedding angle $\theta$ is equal to 30° and 60°, the shale sample experiences shear failure predominantly, characterized by Type II shear cracks, Type III mixed shear cracks and multiple Type IV composite tensile-shear cracks propagating along the bedding planes and penetrating the matrix. As the peak stress intensity escalates, the failure modes of the 30° and 60° bedded shale samples gradually transition from center-oriented failure towards shear failure along the bedding planes, as depicted in Fig. 17(a-f). In instances of small bedding angles, nearly all cracks within the sample manifest as shear fractures along the bedding planes, often accompanied by localized tensile failures. This observation suggests that crack initiation at bedding planes could be rare, with failures primarily originating within the rock matrix. Fig. 17(g) and (h) elucidate the failure patterns of the rock structures, underscoring the substantial impact of bedding angle alteration. The presence of bedding planes in the rock mass disrupts its homogeneity, causing its strength and deformation failure characteristics to differ significantly from those of ordinary isotropic rocks. This results in pronounced anisotropic behavior. When construction activities are carried out on or within bedded rock masses, both the safety of the construction process and the stability of the facilities may be adversely impacted. Thus, understanding the mechanical properties and deformation mechanisms of such layered rock masses is crucial for ensuring the success and safety of engineering projects.

Fig. 18 shows that when the bedding angle $\theta = 90^\circ$, the sample exhibits tensile and splitting cracks propagating along its bedding planes, ultimately penetrating the sample. With an escalation in peak stress wave intensity, the primary macroscopic cracks within the 90° bedded shale sample remain relatively stable in its fracture characteristics, showing minimal variation. However, there is a noticeable increase in the quantity of small cracks forming between the bedding planes.

## 6. Conclusion

Revealing the fracture characteristics of bedded shales under dynamic impact load is of significant importance for the exploitation and utilization of geological energy. In this study, the progressive failure processes of bedded shale samples were tested by the dynamic SHPB system and measured by the high-speed camera. Furthermore, the related dynamic mechanical properties and fracture features under impact compression inherent in shale formations were comprehensively investigated. The main conclusions drawn from this investigation are outlined as follows:

(1) By meticulously analyzing the triggering mechanisms of micro-cracks and mechanical factors governing fracture morphology, the failure patterns of shale specimens under impact compression can be mainly categorized into five distinct types, *i.e.*, (a) splitting failure along the bedding plane; (b) slip failure along the bedding plane; (c) mixed shear cracks between layers; (d) tensile-shear mixed cracks; (e) tensile crack along the bedding plane.
(2) The dynamic fracture behaviors of shale specimens vary greatly depending on their bedding angles. When the bedding angle $\theta = 0^\circ$, the model experiences a splitting failure that penetrates the bedding planes, with acoustic emissions concentrated predominantly at the horizontal bedding planes. When $\theta = 30^\circ$ and 60°, the shale sample experiences shear failure characterized by shear cracks, mixed shear cracks and multiple composite tensile-shear cracks propagating along the bedding planes and

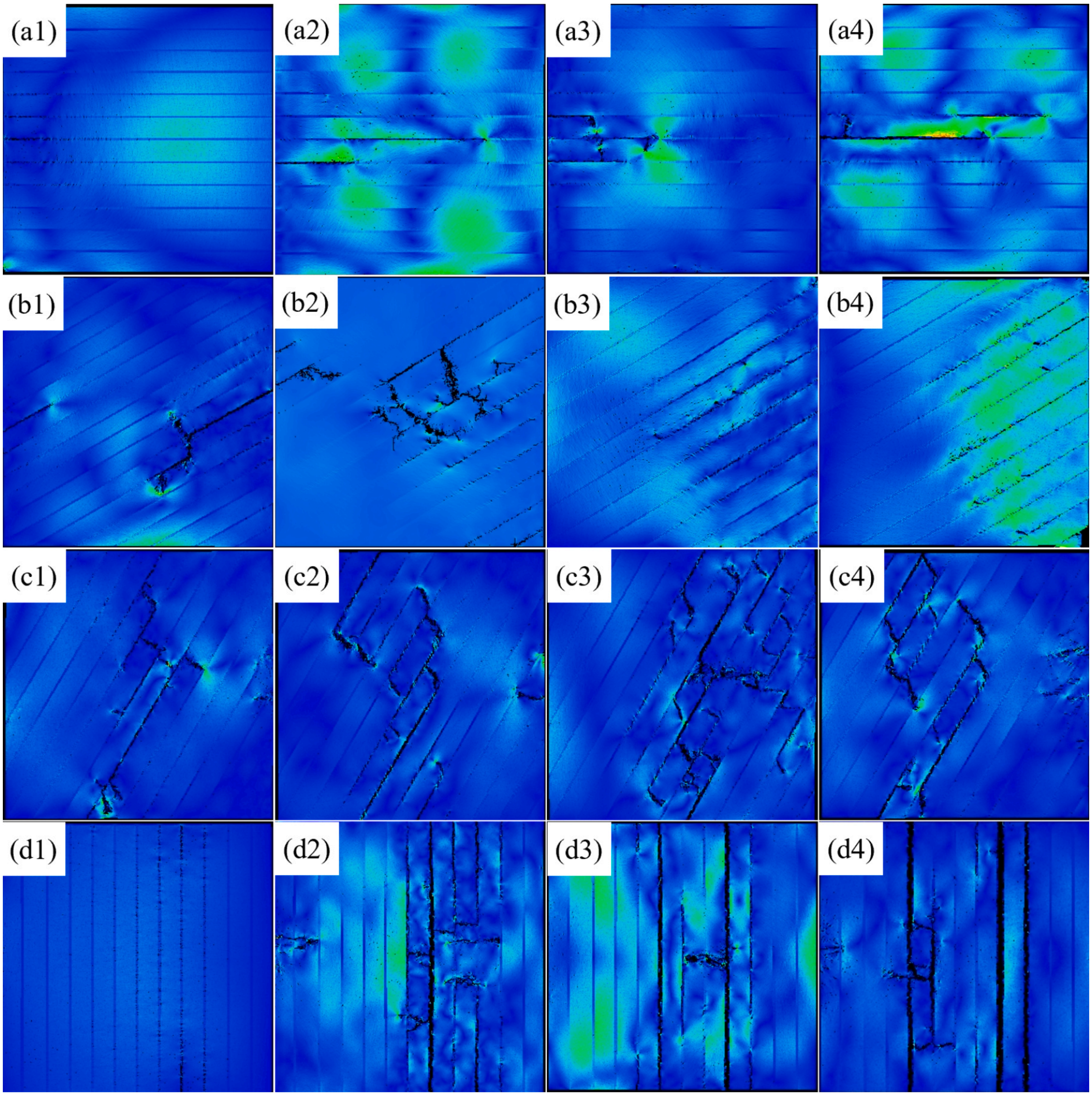


**Fig. 15.** The failure modes represented by the shear stress contours: Series (a), (b), (c) and (d) are for the specimens with $\theta = 0^\circ$, 30°, 60° and 90°, respectively; Series (1), (2), (3) and (4) correspond to the stress waves 4, 3, 2, and 1, respectively.

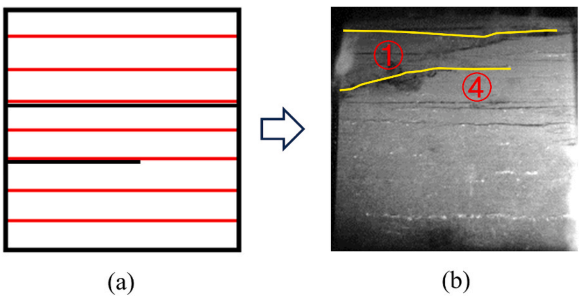


**Fig. 16.** Fracture characteristics of the shale sample with the bedding angle of 0°: (a) schematic Type I cracks and (b) cracks observed in test.

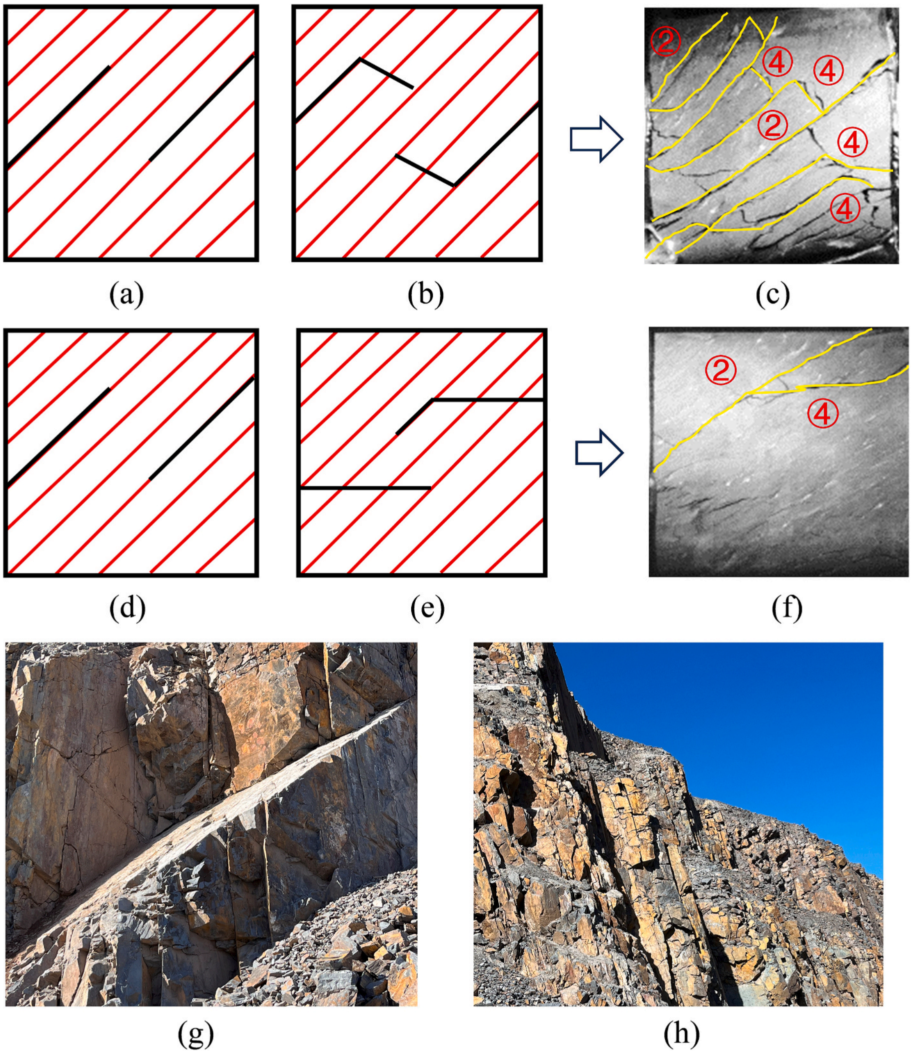


**Fig. 17.** Failure characteristics of the rock mass with inclined structural planes: (a-b), (d-e) schematic Type II, Type III and Type IV cracks; (c), (f): cracks observed in test; (g-h) cracks observed on-site.

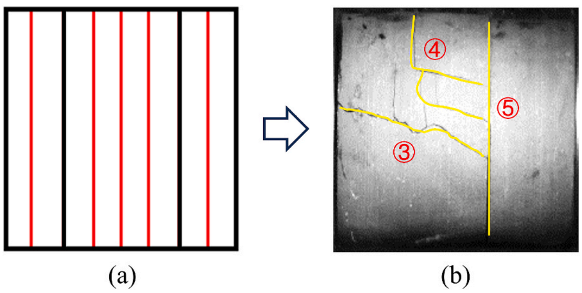


**Fig. 18.** Fracture characteristics of the shale sample with the bedding angle of 90°: (a) schematic Type V cracks and (b) cracks observed in test.

penetrating the matrix. When $\theta = 90^{\circ}$, the sample exhibits tensile and splitting cracks propagating along its bedding planes, ultimately penetrating the sample.

(3) With increasing the strain rate, the fracture modes of shale samples show significant differences. The fracture pattern of 60° bedded specimen lack consistency under various strain rates. Specifically, when the strain rate $\dot{\varepsilon} = 20\ \mathrm{s}^{-1}$, the fracture surface primarily extends along the bedding planes with shear cracks. When $\dot{\varepsilon} = 50\ \mathrm{s}^{-1}$, shear cracking prevails, accompanied by tensile

cracks. With continuously increasing $\dot{\varepsilon}$, the fracture pattern becomes dominated by a combination of slip and tensile-shear mixed cracks.

(4) The loaded waveform has a great influence on the failure patterns of shale samples. As the peak stress intensity escalates, the failure modes of the 30° and 60° bedded shale samples gradually transition from center-oriented failure towards shear failure along the bedding planes. Meanwhile, the 90° bedded specimen exhibits an initial crack along the bedding planes. As the shock wave intensifies, secondary splitting cracks emerge in the matrix, indicative of a fracture pattern across the bedding planes.

## CRediT authorship contribution statement

**Xianhui Feng:** Writing – original draft, Investigation, Funding acquisition, Formal analysis. **Bin Gong:** Writing – review & editing, Supervision, Methodology, Funding acquisition, Conceptualization. **Xiaofeng Cheng:** Writing – review & editing, Investigation, Data curation. **Xu Chen:** Writing – review & editing, Visualization, Formal analysis. **Xun Xi:** Funding acquisition, Formal analysis. **Kaikai Wang:** Validation, Formal analysis.

## Funding

The present work was financially supported by the Beijing Natural Science Foundation, China (Grant No. 2244099), the China Postdoctoral Science Foundation, China (Grant No. 2023TQ0025) and the National Natural Science Foundation of China, China (Grant Nos. 42107208, 52304077).

## Declaration of competing interest

The authors declare that they have no known competing financial interests or personal relationships that could have appeared to influence the work reported in this paper.

## Data availability

Data will be made available on request.

## References

[1] Feng X, Gong B, Tang C, Zhao T. Study on the non-linear deformation and failure characteristics of eps concrete based on ct-scanned structure modelling and cloud computing. Engng Fract Mech 2022;261:108214.
[2] Feng X, Gong B, Cheng X, Zhang H, Tang C. Anisotropy and microcrack-induced failure precursor of shales under dynamic splitting. Geomat Nat Haz Risk 2022;13(1):2864–89.
[3] Vorobiev OY, Rubin MB. Modeling the dynamic response of rock masses with multiple compliant fluid saturated joint sets—Part I: mesoscale simulations. Int J Impact Eng 2021;151:103747.
[4] Lee J, Lumley DE. Predicting shale mineralogical brittleness index from seismic and elastic property logs using interpretable deep learning. J Pet Sci Eng 2023;220(Part A):111231. https://doi.org/10.1016/j.petrol.2022.111231.
[5] Liang M, Wang Z, Zhang Y, Greenwell CH, Li H, Yu Y, et al. Experimental investigation on gas permeability in bedding shale with brittle and semi-brittle deformations under triaxial compression. J Pet Sci Engng 2021;196:108049.
[6] Tuzingila RM, Kong L, Kasongo RK. A review on experimental techniques and their applications in the effects of mineral content on geomechanical properties of reservoir shale rock. Rock Mech Bull 2024;3(2):100110.
[7] Khmelinin AP, Konurin AI, Denisova EV. Simulation of electromagnetic high-frequency wave propagation processes in multilayer geo-structures. Geohazard Mechanics 2023;1(3):203–7.
[8] Luo N, Zhang H, Chai Y, Li P, Zhai C, Zhou J, et al. Research on damage failure mechanism and dynamic mechanical behavior of layered shale with different angles under confining pressure. Deep Underground Sci Engng 2023;2(4):337–45.
[9] Yu J, Gong B, Cao C, Tang C. A novel cohesive interlayer model considering friction. Int J Solids Struct 2024;305:113049.
[10] Zhang C, Zhu Z, Wang S, Ren X, Shi C. Stress wave propagation and incompatible deformation mechanisms in rock discontinuity interfaces in deep-buried tunnels. Deep Underground Sci Engng 2022;1(1):25–39.
[11] Alhemdi A, Gu M. Method to account for natural fracture induced elastic anisotropy in geomechanical characterization of shale gas reservoirs. J Nat Gas Sci Engng 2022;101:104478.
[12] Liu L, Zhang Z, Wang T, Zhi S, Wang J. Evolution characteristics of fracture volume and acoustic emission entropy of monzogranite under cyclic loading. Geomech Geophys Geo-Energy Geo-Resour 2024;10:16.
[13] Ma T, Wang H, Liu Y, Fu C, Ranjith PG. Experimental investigation on the anisotropy of mode-I fracture and tensile failure of layered shale. Engng Fract Mech 2023;290:109484.
[14] Leroy MNL, Joseph N, Bienvenu NJM. Redistribution and magnitude of stresses around horse shoe and circular excavations opened in anisotropic rock. Int J Min Sci Technol 2015;25(4):615–21.
[15] Nguyen TS, Tanapalungkorn W, Likitlersuang S. Probabilistic analysis of dual circular tunnels in rock masses considering rotated anisotropic random fields. Comput Geotech 2024;170:106319.
[16] Wang Y, Chen Q, Dai B, Wang D. Guidance and review: Advancing mining technology for enhanced production and supply of strategic minerals in China. Green and Smart Mining Engineering 2024;1(1):2–11.
[17] Luo N, Fan X, Cao X, Zhai C, Tao HT. Dynamic mechanical properties and constitutive model of shale with different bedding under triaxial impact test. J Pet Sci Engng 2022;216:110758.
[18] Luo P, Li D, Zhou A, Ma J, Zhu Q, Jiang J. Influence of bedding plane on the tensile properties and crack propagation of soft and hard laminated rock-like under Brazilian test. Theor Appl Fract Mech 2023;127:104087.
[19] Chao Z, Shi D, Zheng J. Experimental research on temperature-dependent dynamic interface interaction between marine coral sand and polymer layer. Ocean Engng 2024;297:117100.
[20] Zhang Y, Chen S, Zhai X, Khan J, Zhang Y. Brazilian splitting experiment and finite element simulation analysis of the influence of bedding loading angle on shale fracture mode. Nat Gas Ind B 2023;10(6):602–12.

[21] Kolawole O, Oppong F. Assessment of inherent heterogeneity effect on continuous mechanical properties of shale via uniaxial compression and scratch test methods. Rock Mech Bull 2023;2(4):100065.
[22] Zhang Y, Zhao Y, Long A, Wang C, Bi J. Combined effects of bedding anisotropy and matrix heterogeneity on hydraulic fracturing of shales from Changning and Lushan, South China: an experimental investigation. J Asian Earth Sci 2024;259:105908.
[23] Zhao C, Liu J, Lyu C, Liang C, Xu D, Ren Y. Mechanical responses and failure characteristics of longmaxi formation shale under real-time high temperature and high-stress coupling. Engng Fail Anal 2023;152:107490.
[24] Zhou X, Han L, Bi J, Shou Y. Experimental and numerical study on dynamic mechanical behaviors of shale under true triaxial compression at high strain rate. Int J Min Sci Technol 2024;34(2):149–65.
[25] Wu Y, Ma D, Hu X, Hao Y, Liu C, Zhou H. Numerical simulation on the mechanical and fracture behavior of bedding argillaceous sandstone containing two pre-existing flaws. Theor Appl Fract Mech 2023;127:104047.
[26] Zhai M, Xue L, Bu F, Yang B, Huang X, Liang N, et al. Effects of bedding planes on progressive failure of shales under uniaxial compression: Insights from acoustic emission characteristics. Theor Appl Fract Mech 2022;119:103343.
[27] Wang P, Ma C, Liu C, Liu Q, Fu Y, Cai M. Anisotropic behavior of excavated layered rock mass subjected to compression considering the joint roughness. Bull Engng Geol Environ 2023;82(10):373.
[28] Wang P, Ma C, Zhang B, Gou Q, Tan W, Cai M. Development of an improved three-dimensional rough discrete fracture network model: method and application. Int J Min Sci Technol 2023;33(12):1469–85.
[29] Aminzadeh A, Fahimifar A, Nejati M. On Brazilian disk test for mixed-mode I/II fracture toughness experiments of anisotropic rocks. Theor Appl Fract Mech 2019;102:222–38.
[30] Cai X, Cheng C, Zhou Z, Konietzky H, Song Z, Wang S. Rock mass watering for rock-burst prevention: some thoughts on the mechanisms deduced from laboratory results. Bull Engng Geol Environ 2021;80(11):8725–43.
[31] Li D, Ma J, Wan Q, Zhu Q, Han Z. Effect of thermal treatment on the fracture toughness and subcritical crack growth of granite in double-torsion test. Engng Fract Mech 2021;253:107903.
[32] Zhu Q, Li D, Han Z, Xiao P, Li B. Failure characteristics of brittle rock containing two rectangular holes under uniaxial compression and coupled static-dynamic loads. Acta Geotech 2022;17:131–52.
[33] Li Z, Li L, Huang B, Zhang L, Li M, Zuo J, et al. Numerical investigation on the propagation behavior of hydraulic fractures in shale reservoir based on the DIP technique. J Pet Sci Engng 2017;154:302–14.
[34] Yu Q, Liu H, Yang T, Liu H. 3D numerical study on fracture process of concrete with different ITZ properties using X-ray computerized tomography. Int J Solids Struct 2018;147:204–22.
[35] Meng Y, Jing H, Liu X, Yin Q, Wei X. Experimental and numerical investigation on the effects of bedding plane properties on the mechanical and acoustic emission characteristics of sandy mudstone. Engng Fract Mech 2021;2021(245):107582.
[36] Wang P, Cai M, Ren F. Anisotropy and directionality of tensile behaviours of a jointed rock mass subjected to numerical Brazilian tests. Tunnelling and Underground Space Technology incorporating Trenchless Technology Research 2018;73:139–53.
[37] Gong B, Zhao T, Thusyanthan I, Tang C, Zhou GGD. Integrating RFPA and DEM in adaptive RDFA modeling of rock fracturing process. Rock Mech Rock Engng 2025;58:2569–87.
[38] Chen BP, Gong B, Wang SY, Tang CA. Research on zonal disintegration characteristics and failure mechanisms of deep tunnel in jointed rock mass with strength reduction method. Mathematics 2022;10(6):922.
[39] Liu X, Gong B, Song K, Liu H. Indirect tensile strength test on heterogeneous rock using square plate sample with a circular hole. Lithosphere 2024;2024(3): lithosphere_2023_322.
[40] Tang CA, Webb AAG, Moore WB, Wang YY, Ma TH, Chen TT. Breaking Earth's shell into a global plate network. Nat Commun 2020;11(1):3621.
[41] Gong B, Wang Y, Chen X, Song W, Wang K, Yu J. Analysis of sensitivity factors on CJB mechanical behavior from specimen scale to engineering scale. Engng Fract Mech 2025;314:110673.
[42] Wang Y, Gong B, Tang C, Yang X. Size effect and lateral pressure effect on the mechanical resistance of columnar jointed basalt. Int J Rock Mech Min Sci 2023;171:105571.
[43] Gong B, Zhao T, Thusyanthan I, Tang C, Zhou GGD. The random RFPA method for modelling rock failure. Rock Mech Rock Engng 2025. https://doi.org/10.1007/s00603-025-04400-3.
[44] Gong B, Zhao T, Thusyanthan I, Tang C. Modelling rock fracturing by a novel implicit continuous to discontinuous method. Comput Geotech 2024;166:106035.
[45] Feng X, Gong B, Liang Z, Wang S, Tang C, Li H, et al. Study of the dynamic failure characteristics of anisotropic shales under impact Brazilian splitting. Rock Mech Rock Engng 2024;57:2213–30.
[46] Liu H, Feng X, Liu L, Li T, Tang C. Mechanical properties and failure characteristics of anisotropic shale with circular hole under combined dynamic and static loading. Int J Rock Mech Min Sci 2023;170:105524.